A Microwave-Based Sensing Platform for Microplastic Detection and Quantification: A Machine Learning-Assisted Approach

Mateus I. O. Souza, Leonardo Tarczewski, Brian N. Lahr, Achiles F. da Mota, Andrei Leitão, Vinicius M. Pepino, *Member, IEEE*, and Ben-Hur V. Borges

***Abstract*—This work introduces a low-cost microwave (MW) sensor that achieves the highest sensitivity among MW-based approaches for detecting microplastics (MPs) in water and provides a mechanism for determining polymer types in unknown samples. These achievements address the growing need for sensitive, affordable tools for routine and reliable monitoring of MPs across environmental water matrices. We employ an MW spiral resonator operating at 3.4 GHz to detect and quantify polytetrafluoroethylene (PTFE), polyvinyl chloride (PVC), and polyethylene terephthalate (PET) in water. The design leverages a highly sensitive spoof surface plasmon polariton (SSPP) mode and a controlled field–sample interaction, enabling tunable coupling and robustness to variations in sample composition. Under maximum interaction (1.6-mL sample volume), the resonator detects concentrations as low as 125 ppm for all polymers. To overcome overlapping responses from similar dielectric properties, we integrate machine learning (ML) to discriminate polymer type. Four algorithms, random forest (RF), K-nearest neighbors (KNNs), support vector machine (SVM), and logistic regression (LR), were evaluated using resonance-derived features: frequency shift, minimum amplitude, 3-dB bandwidth, and skewness. LR achieved the best performance, correctly classifying 100% of samples. After identification, polymer-specific calibration curves are used to estimate the concentration. These findings establish the platform as a sensitive, selective, and low-cost solution for MP monitoring in water. By coupling SSPP-enabled sensing with ML-based classification, this work advances the state of the art in MW environmental monitoring and offers a practical route for addressing MP pollution while enabling both quantification and identification in a single device.**

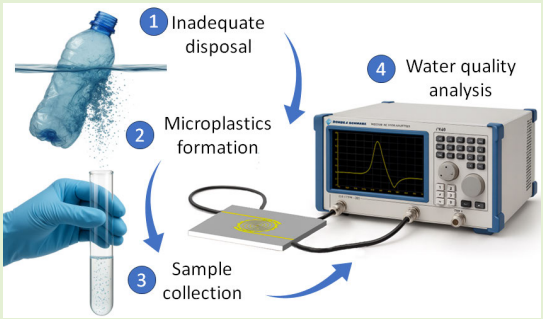

***Index Terms*—Classification, machine learning (ML), microplastic (MP), microwave (MW), sensor, spoof surface plasmon polariton (SSPP).**

I. Introduction

PLASTICS have become deeply embedded in modern society due to their low cost, durability, and versatility, enabling widespread use across industries such as packaging, healthcare, and transportation [1]. However, the same properties that make plastics so useful, particularly their resistance to degradation, also contribute to their long-term persistence in the environment. Today, global plastic production exceeds 359 million tons annually, driven in large part by single-use applications and inadequate disposal practices [2]. Common sources of plastic waste include textiles, tires, water bottles, and personal care products such as cosmetics [3].

As plastic waste accumulates in natural environments, it undergoes physical, chemical, and biological degradation processes that lead to the formation of microplastics (MPs). These are polymer fragments ranging in size from 1 μm to 5 mm [4] and have been detected in aquatic systems, soil, and even within living organisms. The growing prevalence of MPs in the environment has raised serious concerns due to their potential to disrupt ecosystems and pose risks to human health. Human exposure occurs primarily through dermal contact, inhalation, and ingestion, the latter two being the most significant pathways [5]. Among these, inhalation of airborne MPs

Received 28 January 2026; revised 16 February 2026; accepted 16 February 2026. Date of publication 26 February 2026; date of current version 2 April 2026. This work was supported in part by the Coordination for the Improvement of Higher Education Personnel (CAPES) under Grant 001, in part by the National Council of Scientific and Technological Development (CNPq) under Grant 304208/2021-3 and Grant 312086/2023-7, and in part by São Paulo Research Foundation (FAPESP) under Grant 2013/07276-1 and Grant 2023/16111-8. The work of Vinicius M. Pepino was supported by FAPESP under Grant 2025/09387-2. The associate editor coordinating the review of this article and approving it for publication was Prof. Mohammad Hossein Zarifi. *(Corresponding author: Ben-Hur V. Borges.)*

Please see the Acknowledgment section of this article for the author affiliations.

This article has supplementary downloadable material available at https://doi.org/10.1109/JSEN.2026.3666661, provided by the authors.

Digital Object Identifier 10.1109/JSEN.2026.3666661

is considered the main route, followed by the consumption of seafood and bottled water [6]. The confirmed presence of MPs in human tissues and their associated health risks [7], [8], [9], [10] have intensified the need for water-quality monitoring systems aimed at protecting human health.

Sensor-based approaches for MP analysis have focused on parameters such as particle count [11], concentration [12], size distribution [13], and polymer identification [14]. Other strategies target MP removal [15] or seek to differentiate MPs from biological materials [16]. The primary technologies employed for these analyses include Fourier transform infrared (FTIR) spectroscopy [14], [17], Raman spectroscopy [18], [19], and microwave (MW) spectroscopy [12], [13], [20], [21], [22], [23]. FTIR enables rapid, nondestructive identification of functional groups in liquids [24], but its applicability is limited by strong water absorption [25] and shallow penetration depth [26]. Raman spectroscopy overcomes water-related constraints [27] and provides molecular fingerprints [28], yet its weak scattering efficiency [29], susceptibility to fluorescence interference [30], and high system cost [31] often require long acquisition times or signal enhancement, restricting its practical deployment.

MW sensors rely on permittivity-induced perturbations of planar resonators, which manifest as shifts in the measured S-parameters [32]. In MP detection, polymers modify the effective permittivity of the water matrix, leading to changes in resonance features such as frequency shift (Δf), attenuation (ΔA), and quality factor (ΔQ). MW sensors present several noteworthy advantages: label-free operation [33], noncontact measurements [34], and high sensitivity to even minor dielectric changes [35]. Moreover, they are compact, cost-effective [36], and readily manufactured using standard printed circuit board (PCB) fabrication processes. Collectively, these attributes position MW sensors as strong candidates for detecting low MP concentrations in water while helping to overcome some of the key limitations inherent to FTIR and Raman-based methods.

Previous studies have demonstrated the versatility of MW-based sensing for MP detection across diverse media. In [20], Nylon 11 was identified in liquid samples as well as in soil and sand, highlighting the relevance of MW techniques beyond aquatic environments. In [37], PP and PE particles were analyzed in distilled water, artificial sewage, and urban lake water to assess matrix-dependent effects on detection performance. In [12], 10-μm PP, PMMA, and polyethylene terephthalate (PET) particles were investigated, showing that particle shape had no measurable influence on resonance frequency shifts. In [38], an adaptable MW resonator integrating a microfilter was proposed for on-site PP concentration estimation. A low-cost MW system combining a signal generator and spectrum analyzer was reported in [21], enabling PP and PE detection down to 1% concentration without a vector network analyzer (VNA). In [22], a split-ring resonator was used to study the effects of particle size, concentration, and temperature on PE suspensions, achieving a detection limit of 100 000 particles/L. Finally, a real-time MW probe reported in [23] detected 600-μm PE spheres, albeit at substantially larger particle sizes than those addressed in most studies.

Despite ongoing efforts to enhance MW sensor performance, their sensitivity remains below that of FTIR and Raman techniques. Moreover, no MW-based approach has jointly addressed polymer-type identification and concentration quantification in unknown MP samples. Here, we address this gap by proposing: 1) a high-sensitivity spoof surface plasmon polariton (SSPP) resonator for MP detection in water and 2) a machine learning (ML) strategy for polymer identification in unknown samples.

SSPP-based resonant sensors enable strong field confinement for MW sensing. Label-free detection has been demonstrated for pollutant monitoring in sewage water [39], multifunctional sensing of alcohol concentration and paper thickness [40], and portable gas detection using ultracompact, consumer-electronics-integrated platforms [41]. Biomedical applications include glucose sensing in blood phantoms and aqueous solutions [42], [43], while microfluidic SSPP sensors have enabled food-quality analysis such as honey adulteration detection [44]. Recent advances further include flexible SSPP e-skins for proximity and material identification [45]. Overall, these works establish SSPP resonators as a mature and versatile sensing technology.

Herein, we designed a spiral SSPP resonator and mapped its response as a function of sample volume, a key determinant of sensor–sample coupling. At the optimal 1.6-mL volume, the device detected polytetrafluoroethylene (PTFE), polyvinyl chloride (PVC), and PET down to 0.0125% (125 ppm) with low error, surpassing prior MW-based reports. For polymer identification, four models, random forest (RF), K-nearest neighbors (KNNs), support vector machine (SVM), and logistic regression (LR), were trained using four experimentally measured features: resonance frequency ($f_{\min}$), transmission amplitude ($S_{21,\min}$), 3-dB bandwidth (B_{width}), and skewness (SK_{ness}). LR achieved 100% accuracy on our dataset, correctly classifying all samples. Together, these results indicate a robust route to MP detection and classification in water.

This article is organized as follows. Section II describes the MP sensing concept and sensor design, including a sample volume analysis. The corresponding results are experimentally validated in Section III. Section IV details the sample preparation and the resonator response for PTFE, PVC, and PET, dispersed in deionized water (DI-W). Section V introduces the ML models and evaluates their predictive capability for the three polymers, including a comparison of the proposed sensor with other MW approaches. Finally, Section VI summarizes the main findings.

II. MP Sensing Methodology and Design

Fig. 1 summarizes our MW workflow for MP analysis in water, organized in four stages. First, samples are collected at treatment facilities or directly from natural sources. Second, the sample is placed in the sensor and its frequency response is measured, and the relevant resonance-based features ($f_{\min}$, $S_{21,\min}$, B_{width}, and SK_{ness}) are extracted from the transmission coefficient. Third, these features are used as inputs to a supervised classification model to identify the polymer type (PTFE, PVC, or PET) and select the corresponding regression curve. Fourth, the concentration of the identified

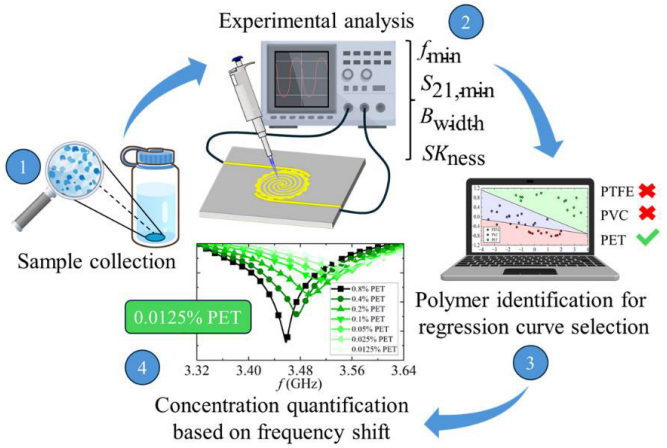

Fig. 1. Overview of the experimental workflow for MP analysis. (1) MP samples are prepared and introduced into the sensor setup. (2) Scattering parameters are measured using a VNA, and the relevant resonance-based features are extracted. (3) The extracted features are used as inputs to a supervised classification model for polymer identification and regression curve selection. (4) Based on the selected regression curve, the MP concentration is quantified using the resonance frequency shift.

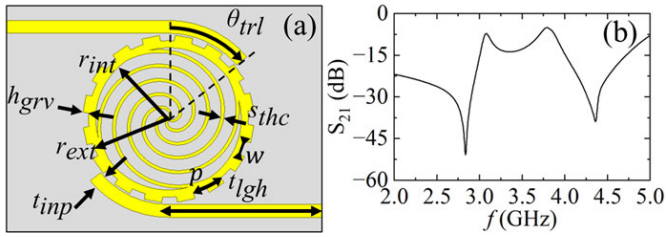

Fig. 2. Proposed spiral resonator and HFSS simulation. (a) Geometry of the Archimedean spiral resonator coupled to a curved transmission line. (b) Simulated transmission coefficient, showing two distinct resonance modes.

polymer is quantified based on the resonance frequency shift using the selected curve.

The proposed sensor uses a spiral resonator whose outer arms are connected to a 16-tooth, gear-shaped ring resonator. The structure is excited by a curved transmission line to maximize coupling, as illustrated in Fig. 2(a). The geometry evolves from previously published spiral-based sensors [46], [47], which have shown promising sensing performance. Spiral resonators provide a highly sensitive near-field region around their arms, strongly coupled through the continuous metallic trace. The resonator follows an Archimedean spiral, implemented as four identical spirals rotated by 90° relative to each other. All geometric parameters of the gear and spiral are provided in the Supplemental Items (SIs), Section A.

The periodic grating on the ring resonator supports an SSPP mode, whose dispersion is engineered via the parameters r_{ext} and h_{gvr} and is used to satisfy the phase-matching condition with a whispering gallery mode (WGM), which is naturally induced in the liquid sample due to its circular geometry. This SSPP-WGM coupling enhances electric-field confinement in the sensing region, with the resulting sensitivity arising from perturbations in this interaction, as detailed in the SI, Section B.

The resonator is not electrically connected to the transmission line, and both are separated by a 150-μm gap to allow electromagnetic coupling. Electromagnetic simulations were performed in HFSS considering the FR-4 substrate. Fig. 2(b) shows the sensor transmission magnitude response, where each resonance peak corresponds to a different mode. Although these modes are sensitive to permittivity variations, the simulation without a test sample does not reflect realistic MP detection conditions. We therefore introduce a sample container and systematically vary the sample volume to quantify its effect on sensor–sample coupling. The 3-D-printed sample container was added to the model to emulate the measurement conditions, positioned directly above the resonator, fully covering it [Fig. 3(a)]. Water at 20 °C served as the analyte, with its permittivity taken from [48].

Because water permittivity dominates the stack, the sample volume primarily governs the sensor response. An initial height, $h_{\text{sample}} = 3.2$ mm, sufficient for homogeneous filling (∼1.2 mL), yields the magnitude response in Fig. 3(b), where four resonances are observed (black curve with square symbols). The first two correspond to the resonances in Fig. 2(b), shifted due to liquid loading, whereas the third and fourth arise as higher order SSPP modes enabled by the presence of water (further analysis is provided in the SI). To assess dielectric sensitivity, a perturbation of $\Delta\varepsilon' = -5$ was applied in the whole band while keeping dielectric losses constant. The resulting response is shown by the red curve with circular symbols, highlighting the corresponding frequency shifts. As observed, the third and fourth resonances exhibit higher sensitivity and were therefore selected for analysis. For volume comparison, narrow sweeps around each resonance were simulated, see Fig. 3(c) and (d), for $h_{\text{sample}} = 3.0$–3.3 mm. The 2.9-GHz mode was essentially invariant (low sensitivity), while the 3.3-GHz mode shifted markedly with volume. Therefore, considering the high sensitivity, enhanced quality factor, and the coupled-mode-based sensing mechanism, the analysis was focused exclusively on the resonance centered at 3.3 GHz. The best performance occurred at $h_{\text{sample}} = 3.1$ mm (∼1.2 mL), yielding the deepest attenuation and the highest Q across all tested volumes.

Fig. 4 shows the electric-field distribution, with maximum intensity near the water surface and gradual decay with depth, while the xy plane views confirm strong confinement between the transmission line and resonator. This behavior supports MP detection via permittivity-induced resonance perturbations. The distinct substrate field pattern confirms SSPP excitation by the grating and the associated coupling mechanism (see SI, Section C). Sensor fabrication and experimental validation are the next steps.

III. Sensor Fabrication and Experimental Validation

The sensor was fabricated via electronic prototyping, using an LPKF milling machine (model S-103), with 1.6-mm-thick FR-4 ($\varepsilon_r = 4.4 - j0.08$) as the substrate material. Two SMA connectors were soldered to each port. A cylindrical sample container was also fabricated, featuring walls made of 3-D-printed resin ($\varepsilon_r = 2.7 - j0.08$) and a base consisting of a 150-μm glass layer ($\varepsilon_r = 5.5 - j0$) [49]. The container is

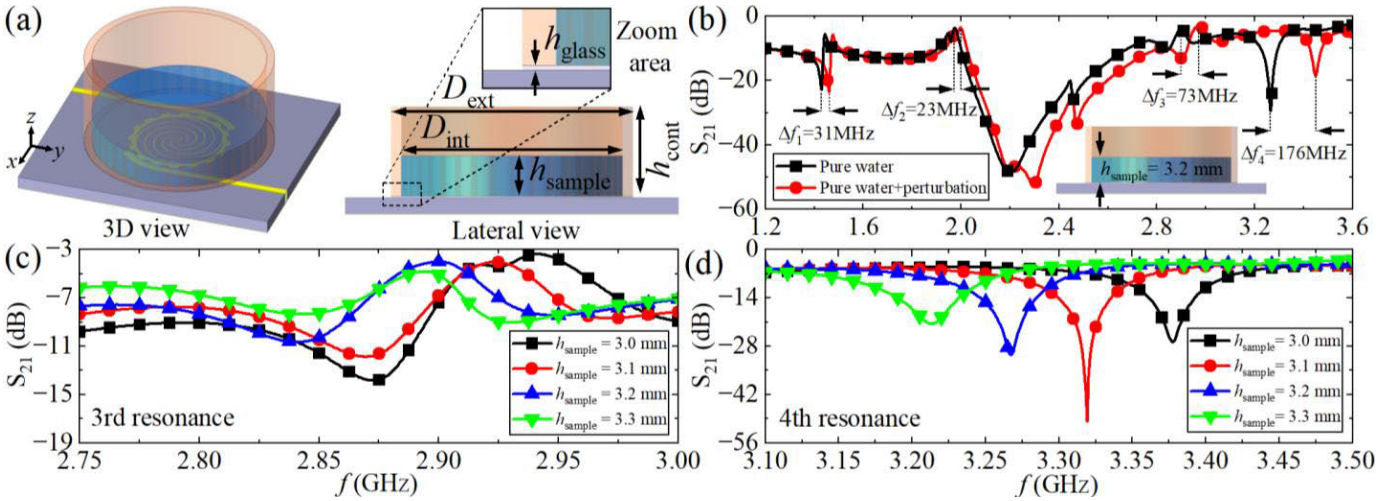

Fig. 3. Simulation-based sensitivity analysis of the spiral resonator using pure water. (a) Sensor geometry and container dimensions. (b) Simulated transmission coefficient for a 3.2-mm-high water sample with and without dielectric perturbation ($\Delta\varepsilon' = -5$), used for sensitivity assessment. (c) and (d) Sensitivity fine-tuning for different sample volumes at the third and fourth resonances.

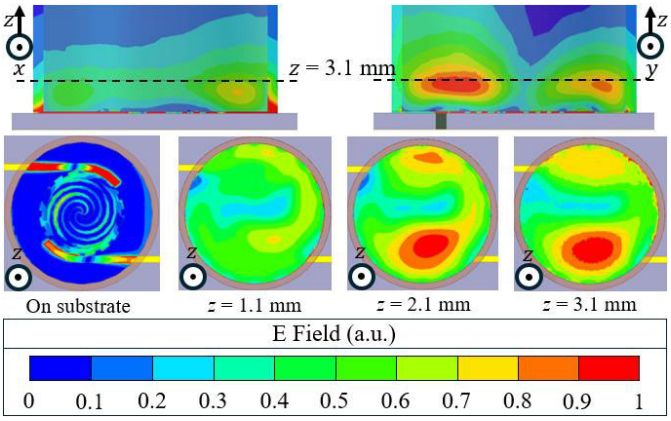

Fig. 4. Simulated electric-field distribution at $z = 3.1$ mm. Top: xz and yz cross sections; bottom: xy intensity maps. Strong field confinement within the liquid indicates high dielectric sensitivity.

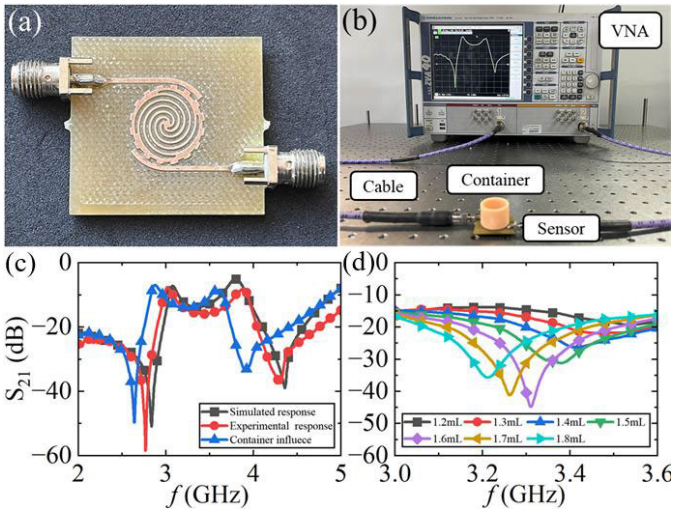

Fig. 5. Fabrication, measurement setup, and experimental validation of the SSPP sensor. (a) Fabricated resonator. (b) Measurement setup. (c) Simulated and measured transmission magnitude responses. (d) Measured response for varying water volumes.

16.4 mm tall, with the inner diameter of 22 mm and the outer diameter of 24 mm.

The fabricated structure is shown in Fig. 5(a), where the element appears connected to a ZVA-40 Rohde and Schwarz VNA in Fig. 5(b), in order to replicate the same conditions implemented in the simulations. Fig. 5(c) compares the magnitude of the transmission coefficient for three configurations: the simulated response (black curve with square symbols), the experimental response without the container (red curve with circular symbols), and the experimental response with the container (blue curve with triangular symbols). A good correspondence between the simulated and experimental approaches is observed. The presence of the container causes a redshift of approximately 100 MHz in the sensor resonance, while no significant attenuation effects were detected compared with the experimental curve.

The optimal sample volume was confirmed experimentally using a LabMate Pro micropipette (LMP1000) to control DI-W addition. Starting at 1.2 mL, increments of 0.1 mL were made up to 1.8 mL. As shown in Fig. 5(d) (3.0–3.6 GHz), resonance near 3.3 GHz achieved $Q \approx 12$, the highest among the tested volumes, and the lowest transmission amplitude at 1.6 mL, confirming the best sensing condition. The low Q is associated with the high field confinement in water, which is inherently lossy. The observed discrepancies between numerical and experimental results, such as the sample volume and resonant frequency, arise from effects not captured in the numerical model, including setup-related uncertainties, e.g., glass thickness nonuniformities, container misalignment, and glue layer variations, variations in the complex permittivity of water, and capillary effect along the container walls. Next, the sample preparation protocol and its influence on the sensor performance are addressed.

IV. MP Sample Preparation, Detection, and Quantification

MPs of PTFE, PVC, and PET were produced from pure polymers by washing, mechanical scraping with sandpaper,

and sieving (smallest aperture 149 μm). Particle morphology was verified by scanning electron microscopy (SEM, Leo 440). For concentration control, MPs were weighed on an analytical balance (i-ThermoGA64M, Bel Engineering) and dispersed in DI-W. To stabilize the dispersion (and avoid particle agglomeration), sodium dodecyl sulfate (SDS, anionic), Tween 20 (nonionic), and a commercial neutral detergent were assessed. In addition, 0.1% (w/v) surfactant solutions in DI-W had their complex permittivity compared. The commercial neutral detergent was adopted as the reference since its real and imaginary parts of the permittivity closely match those of the other surfactants. Details on polymer selection, sample preparation procedures, and surfactant analysis are provided in Section D of the SI.

The MP sensing setup, Fig. 5(b), employed a fixed 1.6-mL sample volume of DI-W with 0.1% neutral detergent as reference. Measurements started at 0.8% MP concentration (a suitable starting point to properly cover the concentration range of interest for MP analysis), with particle sizes <250 μm (the majority being smaller than this value, as shown in Fig. S5), with successive dilutions prepared by replacing half of the solution with fresh medium and thoroughly mixing with a micropipette. Dilutions proceeded until no further resonance changes were observed, reaching a detection threshold of 0.0125% (125 ppm), the lowest reported for MW sensors. After each sequence, the container was cleaned with DI-W and cotton before restarting. Air bubbles from surfactant agitation were allowed to dissipate before measurements. The SI provides additional details on the measurement time and sedimentation time in Section E. Each MP type (PTFE, PVC, and PET) was tested independently, with four repetitions per concentration, totaling 84 transmission curves. All measurements were performed using the same VNA, with an IF bandwidth of 100 Hz, 501 points, a sweep time of 8 s, and with no averaging applied.

Fig. 6(a)–(c) shows that the average transmission magnitude, obtained from four repeated measurements, increases as the concentration decreases, followed by a clear resonance blue shift. Moreover, it shows that each polymer occupies a distinct resonance range set by its permittivity. Fig. 6(d)–(f) shows the minimum transmission magnitude, where the error bars represent the standard deviation for each concentration. The average standard deviations were 1.49 dB (PTFE), 1.69 dB (PVC), and 2.25 dB (PET), with the highest variability at 0.8%. For PTFE and PET, 0.8% and 0.4% overlapped, while PVC showed more linear behavior. Although the sensor operates at a low Q, resonance frequencies, see Fig. 6(g)–(i), displayed very low deviations ($\approx$2 MHz for PTFE and PVC, and 3 MHz for PET) under repeated measurements at the same concentration and no overlap with adjacent levels, confirming frequency as a more precise and reliable parameter than magnitude. Therefore, the frequency shift is primarily governed by the mixture's effective permittivity, whereas the variability associated with particle geometry, orientation, and spatial distribution is embedded within the frequency dispersion observed across multiple measurements performed at a fixed concentration [50].

Based on these results, the resonance frequency shift was selected as the primary sensing metric. The average sensitivity $\bar{S}$ was calculated using the following equation:

$$\bar{S} = \frac{|\Delta f_{\min(\mathrm{MHz})}|}{\Delta C_{(\%)}} \tag{1}$$

where $\Delta f_{\min}$ represents the change in resonance frequency relative to the reference concentration of 0.8%, considering its average value and ΔC is the variation in MP concentration. The calculated average sensitivities were $\bar{S}_{\mathrm{PTFE}} = 91.81$ MHz/%, $\bar{S}_{\mathrm{PVC}} = 95.11$ MHz/%, and $\bar{S}_{\mathrm{PET}} = 125.08$ MHz/%, indicating that the sensor exhibits the highest average sensitivity to PET concentrations. The complete differential sensitivity curves, obtained from the fit curves, are provided in the SI, Section F. Additionally, using the procedure defined in the SI, Section G, their limit of detections (LODs) are $LOD_{\mathrm{PTFE}} = 0.0347\%$, $LOD_{\mathrm{PVC}} = 0.0156\%$, and $LOD_{\mathrm{PET}} = 0.0381\%$. Determining these parameters is essential for defining the sensor's operational limits. While the sensor demonstrated excellent performance in quantifying PTFE, PVC, and PET, this work also advances beyond quantification by proposing a strategy for polymer-type identification, as detailed next.

V. Polymer-Type Identification Using ML Models

In MW sensing, different analytes may produce highly similar electromagnetic responses, leading to ambiguous readings that cannot be reliably resolved using single-parameter metrics. To overcome this limitation, multivariate feature-based approaches have been successfully employed in fault-tolerant MW sensing architectures to enhance robustness, resolution, and selectivity [51], [52]. In contrast to these works, where intelligent processing primarily targets metrological performance improvement, the present study applies ML to polymer-type identification in MP samples, which is a prerequisite for accurate concentration estimation based on regression models. Therefore, we trained four ML models, namely, RF, KNN, SVM, and LR, using four scattering-based features obtained from experimental data features: $f_{\min}$, $S_{21,\min}$, B_{width}, and SK_{ness}, where B_{width} indicates the -3-dB bandwidth around the resonance notch. SK_{ness} denotes the sample skewness of the resonance profile vector $\mathbf{x} = [x_1, \ldots, x_N]$ [53], with x_i representing the measured S_{21} magnitude in dB, and is defined as

$$SK_{ness} = \frac{\frac{1}{N}\sum_{i=1}^{N}(x_i - \bar{x})^3}{\left(\frac{1}{N}\sum_{i=1}^{N}(x_i - \bar{x})^2\right)^{3/2}} \tag{2}$$

where $\bar{x}$ refers to the arithmetic mean of the resonance profile samples and N is the number of sampled points. The feature set was intentionally restricted to these four variables to avoid performance degradation due to underparameterization and to avoid excessive dimensionality when adding more features. To evaluate the models' performance, the scikit-learn library in Python was employed. The pipeline began with a standard scaler for Z-score normalization. To further reduce overfitting, a stratified fivefold cross-validation with ten repetitions was

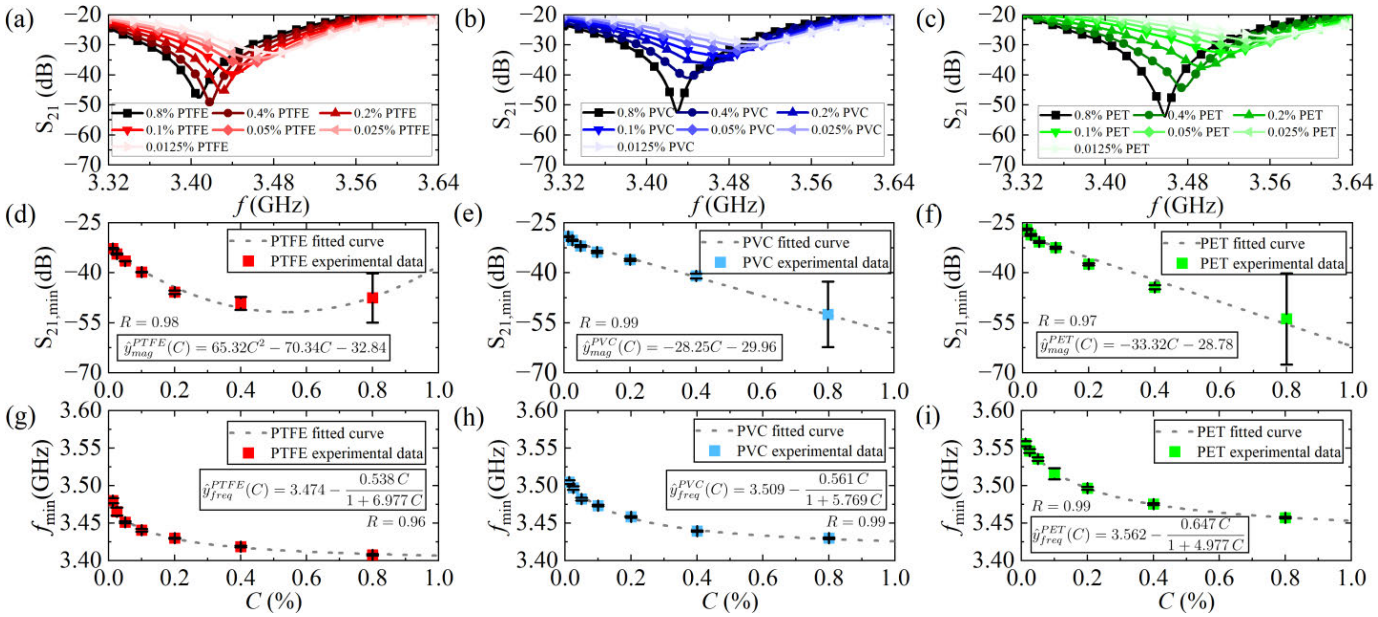

Fig. 6. Averaged experimental S-parameters of the spiral sensor and corresponding fit curves for minimum amplitude and resonance frequency as a function of MP concentration (0.0125%–0.8%) for PTFE, shown in (a), (d), and (g); PVC, shown in (b), (e), and (h); and PET, shown in (c), (f), and (i).

applied. The dataset was expanded fivefold by adding Gaussian noise with a standard deviation set to 10% of each feature's original range, a configuration empirically established to improve generalization while maintaining consistency with the sensor's underlying physics. The dataset was split evenly, with 50% of the real samples used for training and validation, and the remaining 50% reserved for testing. Further discussions on the feature analysis, model testing parameters, and data augmentation procedures are provided in the SI, Section H.

For the performance assessment of the models, three metrics were adopted: validation accuracy ($A_{cc,val}$), test accuracy ($A_{cc,test}$), and an additional metric referred to as adapted accuracy ($A_{cc,adapt}$), defined as

$$A_{cc,adapt}(\%) = \frac{A_{cc,val} + A_{cc,test}}{2}\left(1 - \frac{|A_{cc,val} - A_{cc,test}|}{100}\right). \tag{3}$$

Ranging from 0% to 100%, the adapted accuracy penalizes models with large discrepancies between validation and test performance, particularly those that overfit training data. This is evident for RF and KNN in Fig. 7(a), where shorter bars indicate poor generalization. SVM shows moderate penalization, while LR performs best, confirming the metric's value for robustness evaluation. Despite its simplicity, LR outperformed all other models, suggesting that the relationship between features and polymer classes is largely linear and separable without complex boundaries.

To further examine separability, principal component analysis (PCA) was applied to LR outputs. Fig. 7(b) shows the 2-D projection of sensor features, where PTFE (red), PVC (blue), and PET (green) are clearly distinguished by the classifier. PCA 1 explains 87.97% and PCA 2 8.03% of the variance, indicating that most class-discriminative information lies in a

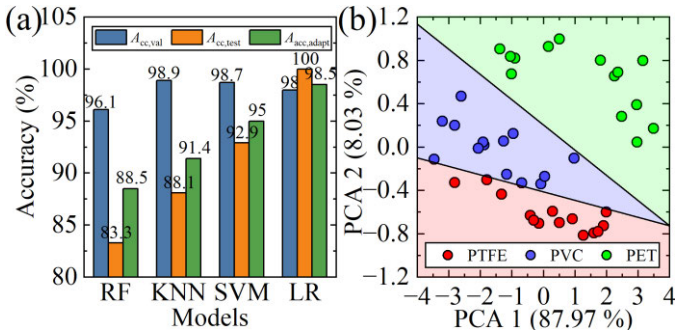

Fig. 7. Performance of ML models for MP classification. (a) Accuracy for RF, KNN, SVM, and LR. (b) PCA projection of LR shows distinct separation among classes.

single dimension, consistent with LR's strong performance. Although dimensionality reduction is feasible, all features were retained to maximize accuracy. The optimal LR used a regularization strength of 100 with the saga solver and 1000 iterations to ensure convergence. These results indicate that our approach is robust to determine the polymer type. Figure S10 in the SI, Section H, summarizes the complete polymer identification process.

Table I summarizes MW sensors for MP detection in water. The proposed sensor operates in the mid-frequency range, balancing sensitivity and precision, and relies on the transmission coefficient, simplifying electronics by avoiding circulators. It belongs to the common MP-dispersed category and, while not requiring the smallest volume, the 1.6-mL sample is practical for water analysis. The device ranks first in the number of MPs analyzed and, unlike most works with fixed sizes, used heterogeneous samples up to 250 μm, with many below 50 μm, better reflecting real conditions. Sensitivity reached 158.7 MHz for 1% MP concentration, while the measured

TABLE I
COMPARISON OF RECENTLY PUBLISHED MP SENSORS USING MW TECHNOLOGY

Ref.	Operating Frequency (GHz)	Measured Variable	MP-Dispersed Medium	Sample Volume (mL)	MP Type	Particle sizes (μm)	Maximum Sensitivity MHz per (%)	Measured Range (%)	Identifying MP in Unknown Samples	Year
[20]	5.2	$\Delta f_{S_{21}}$	No	0.007	Nylon 11	50-500	N.A.	0.5 - 11	No	2020
[38]	2.84	Δf	Yes	0.005	PE	50-500	14.3	2.1 - 94.47	No	2023
[37]	2.05	ΔS_{21}	N.A.	200	PP, PE	200, 250, 500	N.A.	N.A.	No	2023
[12]	4.7	Δf_{S11}	Yes	0.048	PP, PET PMMA	10	10	0 - 4	No	2024
[21]	1.1	$\Delta f_{S_{21}}$	Yes	0.005	PP, PE	33, 50	10, 14	0 - 1	No	2025
[22]	1.15	$\Delta f_{S_{11}}$	Yes	0.1	PE	20, 70	16.7	N.A.	No	2025
[23]	3.72	ΔS_{11}	No	N.A.	PE	600	N.A.	N.A.	No	2025
This Work	**3.32**	$\Delta f_{S_{21}}$	**Yes**	**1.6**	**PTFE, PVC, PET**	**< 250**	**158.7 MHz**	**0.0125-0.8**	**Yes**	**2026**

*N.A.: Not Applicable.

range encompasses the lowest concentration levels reported for MW-based sensors. Additionally, four ML techniques were applied to classify MP type, addressing a key challenge in MW sensing. These results position the sensor at the state of the art, outperforming existing alternatives.

VI. CONCLUSION

This work demonstrated a highly sensitive MW sensing platform for MP quantification and polymer identification in water, enabled by SSPP-based field confinement and ML-learning-assisted classification. Operating at 3.4 GHz, the proposed sensor achieved concentration levels as low as 125 ppm under maximum field–sample interaction (1.6 mL). Using resonance-derived features, the proposed approach enables accurate polymer discrimination, with LR achieving 100% classification accuracy for PTFE, PVC, and PET samples. From an application-oriented perspective, the proposed approach offers a practical route for controlled water analysis, including laboratory screening, bottled water assessment, and periodic monitoring in water treatment facilities, where sample conditions can be properly regulated.

The current laboratory implementation, based on a vector network analyzer, prioritizes measurement fidelity and experimental validation. Building upon this solid foundation, future implementations may leverage compact hardware architectures, such as microprocessor-based platforms and software-defined radio, to enable portable, scalable, and energy-efficient sensing solutions. Controlled sample volume can be reliably ensured using standard laboratory practices, while the ML framework, demonstrated here with three polymer classes, is inherently scalable to larger datasets and more complex classification tasks.

Future work will focus on integrating low-power RF readout electronics, evaluating robustness under realistic water matrices, and expanding the dataset to include a broader range of polymer types and larger sample sets. In this context, the proposed sensing architecture opens a clear pathway toward low-cost, user-friendly devices tailored for practical deployment in this application domain.

ACKNOWLEDGMENT

Mateus I. O. Souza, Brian N. Lahr, Vinicius M. Pepino, and Ben-Hur V. Borges are with the Department of Electrical Engineering and Computing, School of Engineering of São Carlos, University of São Paulo, São Carlos, São Paulo 13566-590, Brazil (e-mail: mateusafk@usp.br; brian.lahr@usp.br; vinicius.pepino@usp.br; benhur@sc.usp.br).

Leonardo Tarczewski and Andrei Leitão are with the Institute of Chemistry of São Carlos, University of São Paulo, São Carlos, São Paulo 13566-590, Brazil (e-mail: tarczewski@usp.br; andleitao@iqsc.usp.br).

Achiles F. da Mota is with the Department of Electrical Engineering, University of Brasilia, Brasilia 70910-900, Brazil (e-mail: achiles.mota@unb.br).

REFERENCES

[1] M. Choudhury and P. Roy, "Challenges with microplastic pollution in the regime of UN sustainable development goals," *World Develop. Sustainability*, vol. 6, Jun. 2025, Art. no. 100216, doi: 10.1016/j.wds.2025.100216.

[2] P. G. C. N. T. Pilapitiya and A. S. Ratnayake, "The world of plastic waste: A review," *Cleaner Mater.*, vol. 11, Mar. 2024, Art. no. 100220.

[3] C. Schmid, L. Cozzarini, and E. Zambello, "Microplastic's story," *Mar. Pollut. Bull.*, vol. 162, Jan. 2021, Art. no. 111820.

[4] N. B. Hartmann et al., "Are we speaking the same language? Recommendations for a definition and categorization framework for plastic debris," *Environ. Sci. Technol.*, vol. 53, no. 3, pp. 1039–1047, Feb. 2019.

[5] P. Wu et al., "Absorption, distribution, metabolism, excretion and toxicity of microplastics in the human body and health implications," *J. Hazardous Mater.*, vol. 437, Sep. 2022, Art. no. 129361.

[6] K. Cox, G. A. Covernton, H. L. Davies, J. F. Dower, F. Juanes, and S. E. Dudas, "Human consumption of microplastics," *Environ. Sci. Technol.*, vol. 53, no. 12, pp. 7068–7074, 2019.

[7] R. Gautam et al., "Evaluation of potential toxicity of polyethylene microplastics on human derived cell lines," *Sci. Total Environ.*, vol. 838, Sep. 2022, Art. no. 156089, doi: 10.1016/j.scitotenv.2022.156089.

[8] T. Luo et al., "Maternal exposure to different sizes of polystyrene microplastics during gestation causes metabolic disorders in their offspring," *Environ. Pollut.*, vol. 255, Dec. 2019, Art. no. 113122, doi: 10.1016/j.envpol.2019.113122.

[9] F. Amereh et al., "Placental plastics in young women from general population correlate with reduced foetal growth in IUGR pregnancies," *Environ. Pollut.*, vol. 314, Dec. 2022, Art. no. 120174.

[10] J. C. Prata, "Airborne microplastics: Consequences to human health?" *Environ. Pollut.*, vol. 234, pp. 115–126, Mar. 2018, doi: 10.1016/j.envpol.2017.11.043.

[11] M. Pollard, E. Hunsicker, and M. Platt, "A tunable three-dimensional printed microfluidic resistive pulse sensor for the characterization of algae and microplastics," *ACS Sensors*, vol. 5, no. 8, pp. 2578–2586, Aug. 2020.

[12] H. Wen et al., "Microfluidic microwave sensor for rapid detection of microplastics in water: Optimization, modeling, and performance evaluation," *IEEE Sensors J.*, vol. 24, no. 21, pp. 35599–35609, Nov. 2024.

[13] Y. C. Alatas, U. Tefek, S. Salehin, H. Alhmoud, and M. S. Hanay, "Rapid differentiation between microplastic particles using integrated microwave cytometry with 3D electrodes," *ACS Sensors*, vol. 10, no. 3, pp. 1729–1735, Mar. 2025.

[14] A. Tan, J. Zhao, Y. Zhao, X. Li, and H. Su, "Determination of microplastics by FTIR spectroscopy based on quaternion parallel feature fusion and support vector machine," *Chemometric Intell. Lab. Syst.*, vol. 243, Dec. 2023, Art. no. 105018.

[15] B. Li, J. Zhao, W. Ge, W. Li, and H. Yuan, "Coagulation-flocculation performance and floc properties for microplastics removal by magnesium hydroxide and PAM," *J. Environ. Chem. Eng.*, vol. 10, no. 2, Apr. 2022, Art. no. 107263.

[16] B. C. Colson and A. P. M. Michel, "Flow-through quantification of microplastics using impedance spectroscopy," *ACS Sensors*, vol. 6, no. 1, pp. 238–244, Jan. 2021.

[17] V. H. da Silva, F. Murphy, J. M. Amigo, C. Stedmon, and J. Strand, "Classification and quantification of microplastics (<100 μm) using a focal plane array–Fourier transform infrared imaging system and machine learning," *Anal. Chem.*, vol. 92, no. 20, pp. 13724–13733, Oct. 2020.

[18] J. Lim, G. Shin, and D. Shin, "Fast detection and classification of microplastics below 10 μm using CNN with Raman spectroscopy," *Anal. Chem.*, vol. 96, no. 17, pp. 6819–6825, 2024.

[19] Y. Luo et al., "Raman spectroscopy and machine learning for microplastics identification and classification in water environments," *IEEE J. Sel. Topics Quantum Electron.*, vol. 29, no. 4, pp. 1–8, Jul. 2023.

[20] O. Malyuskin, "Microplastic detection in soil and water using resonance microwave spectroscopy: A feasibility study," *IEEE Sensors J.*, vol. 20, no. 24, pp. 14817–14826, Dec. 2020.

[21] S.-B. Ku et al., "An RF MEMS sensor driver/readout SoC with resonant frequency shift and closed-loop envelope regulation for portable microplastic detection," *IEEE J. Solid-State Circuits*, vol. 60, no. 5, pp. 1756–1770, May 2025.

[22] P. Zhao et al., "Detection of microplastics by microfluidic microwave sensing: An exploratory study," *Sens. Actuators A, Phys.*, vol. 383, Mar. 2025, Art. no. 116154.

[23] A. Barrancos, V. Macedo, P. M. Ramos, and L. S. Rosado, "Microplastics detection with microfluidics integrated with a microwave sensor," *Meas., Sensors*, vol. 38, May 2025, Art. no. 101435.

[24] J. C. Prata and P. M. da Costa, "Fourier transform infrared spectroscopy use in honey characterization and authentication: A systematic review," *ACS Food Sci. Technol.*, vol. 4, no. 8, pp. 1817–1828, Aug. 2024, doi: 10.1021/acsfoodscitech.4c00377.

[25] B. Chon, S. Xu, and Y. J. Lee, "Compensation of strong water absorption in infrared spectroscopy reveals the secondary structure of proteins in dilute solutions," *Anal. Chem.*, vol. 93, no. 4, pp. 2215–2225, Feb. 2021.

[26] P. K. Krivoshein, D. S. Volkov, O. B. Rogova, and M. A. Proskurnin, "FTIR photoacoustic and ATR spectroscopies of soils with aggregate size fractionation by dry sieving," *ACS Omega*, vol. 7, no. 2, pp. 2177–2197, Jan. 2022, doi: 10.1021/acsomega.1c05702.

[27] S. Klingler, J. Hniopek, R. Stach, M. Schmitt, J. Popp, and B. Mizaikoff, "Simultaneous infrared spectroscopy, Raman spectroscopy, and luminescence sensing: A multispectroscopic analytical platform," *ACS Meas. Sci. Au*, vol. 2, no. 2, pp. 157–166, Apr. 2022, doi: 10.1021/acsmeasuresciau.1c00048.

[28] A. Chandra et al., "Unveiling the molecular secrets: A comprehensive review of Raman spectroscopy in biological research," *ACS Omega*, vol. 9, no. 51, pp. 50049–50063, Dec. 2024, doi: 10.1021/acsomega.4c00591.

[29] R. T. Vulchi, V. Morgunov, R. Junjuri, and T. Bocklitz, "Artifacts and anomalies in Raman spectroscopy: A review on origins and correction procedures," *Molecules*, vol. 29, no. 19, p. 4748, Oct. 2024.

[30] M. R. Kagan and R. L. McCreery, "Reduction of fluorescence interference in Raman spectroscopy via analyte adsorption on graphitic carbon," *Anal. Chem.*, vol. 66, no. 23, pp. 4159–4165, Dec. 1994.

[31] N. Emmanuel, R. B. Nair, B. Abraham, and K. Yoosaf, "Fabricating a low-cost Raman spectrometer to introduce students to spectroscopy basics and applied instrument design," *J. Chem. Educ.*, vol. 98, no. 6, pp. 2109–2116, Jun. 2021, doi: 10.1021/acs.jchemed.0c01028.

[32] M. I. O. Souza, N. M. Santos, J. C. P. Alarcon, L. C. Varanda, V. M. Pepino, and B.-H.-V. Borges, "Microwave glucose sensing using double circular split ring resonators for improved sensitivity: The role of artificial blood plasma and deionized water," *IEEE Sensors J.*, vol. 25, no. 3, pp. 4529–4540, Feb. 2025, doi: 10.1109/JSEN.2024.3516571.

[33] S. Mohammadi, A. V. Nadaraja, K. Luckasavitch, M. C. Jain, D. J. Roberts, and M. H. Zarifi, "A label-free, non-intrusive, and rapid monitoring of bacterial growth on solid medium using microwave biosensor," *IEEE Trans. Biomed. Circuits Syst.*, vol. 14, no. 1, pp. 2–11, Feb. 2020, doi: 10.1109/TBCAS.2019.2952841.

[34] S. Harnsoongnoen and A. Wanthong, "A non-contact planar microwave sensor for detection of high-salinity water containing NaCl, KCl, $CaCl_2$, $MgCl_2$ and Na_2CO_3," *Sens. Actuators B, Chem.*, vol. 331, Mar. 2021, Art. no. 129355.

[35] S. Kiani, P. Rezaei, and M. Navaei, "Dual-sensing and dual-frequency microwave SRR sensor for liquid samples permittivity detection," *Measurement*, vol. 160, Aug. 2020, Art. no. 107805.

[36] F. Jafari and M. Rad Malekshahi, "A low-cost microwave microfluidic sensor based on planar ring resonator," *IEEE Sensors J.*, vol. 23, no. 18, pp. 21070–21077, Sep. 2023.

[37] Y. Liu, X. Xiao, and X.-Y. You, "Detection of low concentration microplastics in water based on the perturbation of the microwave resonance," *Measurement*, vol. 222, Nov. 2023, Art. no. 113633.

[38] K.-H. Lee, J.-H. Kim, K.-S. Shin, C.-U. Cha, and H.-M. Lee, "Complementary multisplit ring resonant MEMS sensor with microfilter for microplastics concentration measurement," *IEEE Sensors J.*, vol. 23, no. 17, pp. 19105–19116, Sep. 2023.

[39] S. Imamvali, T. Nagarajan, R. Chaparala, and S. Tupakula, "Label-free biosensing of persistent organic pollutants in sewage water using spoof surface plasmon polaritons," *Sens. Actuat. A, Phys.*, 2025, doi: 10.1016/j.sna.2025.115365.

[40] K. Ram, R. Singh, and M. J. Akhtar, "A dual functional SSPP based microwave sensor for detecting volumetric concentration of alcohol mixtures and paper thickness," *Microsyst. Technol.*, 2025, doi: 10.1007/s00542-025-05941-7.

[41] Y. Zhang, H. Liu, J. Wang, and Z. Chen, "An ultracompact spoof surface plasmon sensing system for adaptive and accurate detection of gas using a smartphone," *J. Adv. Res.*, 2024, doi: 10.1016/j.jare.2023.10.012.

[42] S. Imamvali, T. Nagarajan, R. Chaparala, and S. Tupakula, "Spoof surface plasmon polaritons-based detection of glucose in blood phantom for medical diagnosis," *IEEE Sensors J.*, 2024, doi: 10.1109/JSEN.2024.3474859.

[43] A. Kandwal, Z. Nie, and Z. Hao, "Surface plasmonic feature microwave sensor with highly confined fields for aqueous-glucose and blood-glucose measurements," *IEEE Sens. J.*, 2021, doi: 10.1109/JSEN.2021.3056421.

[44] S. Imamvali et al., "Microfluidic-integrated SSPP sensor for rapid and sensitive label-free honey adulteration," *J. Magn. Magn. Mater.*, vol. 629, Oct. 2025, Art. no. 173255, doi: 10.1016/j.jmmm.2025.173255.

[45] Y. Li, S. Zhang, X. Li, C. Lee, M. Zhu, and T. Chen, "Spoof surface plasmon polariton enabled flexible e-skin for cross-media proximity sensing and material identification," *ACS Appl. Mater. Interface*, vol. 18, no. 1, pp. 3262–3273, Jan. 2026, doi: 10.1021/acsami.5c20801.

[46] M. I. O. Souza, A. F. D. Mota, V. M. Pepino, J. P. Carmo, and B.-H.-V. Borges, "Multi-purpose microwave biosensor based on signal encoding technique and microfluidics for improved sensitivity," *IEEE Sensors J.*, vol. 21, no. 4, pp. 4571–4581, Feb. 2021, doi: 10.1109/JSEN.2020.3033970.

[47] J. C. P. Alarcon, M. I. O. Souza, V. M. Pepino, and B.-H.-V. Borges, "Identification and quantification of common adulterants in extra virgin olive oil using microwave dielectric spectroscopy aided by feedforward neural networks," *IEEE Sensors J.*, vol. 24, no. 19, pp. 29985–29995, Oct. 2024, doi: 10.1109/JSEN.2024.3448221.

[48] T. Meissner and F. J. Wentz, "The complex dielectric constant of pure and sea water from microwave satellite observations," *IEEE Trans. Geosci. Remote Sens.*, vol. 42, no. 9, pp. 1836–1849, Sep. 2004.

[49] A. R. von Hippel and S. O. Morgan, "Dielectric materials and applications," *J. Electrochemical Soc.*, vol. 102, no. 3, 1955, Art. no. 68Ca, doi: 10.1149/1.2430014.

[50] M. I. O. Souza, N. M. Santos, L. C. Varanda, V. M. Pepino, and B.-H.-V. Borges, "A microwave sensor based on concentric split-ring resonators for blood urea detection: A novel tool for chronic kidney disease diagnosis," *IEEE Sensors J.*, vol. 25, no. 13, pp. 24173–24180, Jul. 2025, doi: 10.1109/JSEN.2025.3570067.

[51] M. Abdolrazzaghi, M. H. Zarifi, W. Pedrycz, and M. Daneshmand, "Robust ultra-high resolution microwave planar sensor using fuzzy neural network approach," *IEEE Sensors J.*, vol. 17, no. 2, pp. 323–332, Jan. 2017, doi: 10.1109/JSEN.2016.2631618.
[52] M. Abdolrazzaghi, N. Kazemi, V. Nayyeri, and F. Martin, "AI-assisted ultra-high-sensitivity/resolution active-coupled CSRR-based sensor with embedded selectivity," *Sensors*, vol. 23, no. 13, p. 6236, Jul. 2023, doi: 10.3390/s23136236.
[53] *Skewness*, MathWorks Inc., Natick, MA, USA, 2025. [Online]. Available: https://www.mathworks.com/help/stats/skewness.html

Mateus I. O. Souza received the Ph.D. degree in electrical engineering from the School of Engineering, University of São Paulo (EESC/USP), São Carlos, Brazil, in 2025.

His research interests include the design of RF resonators, biosensors, signal processing, and machine learning techniques.

Leonardo Tarczewski was born in Curitiba, Paraná, Brazil, in November 2000. He received the bachelor's degree in chemistry from the Federal University of Technology – Paraná (UTFPR), Curitiba. He is currently pursuing the master's degree in chemistry with the Institute of Chemistry of São Carlos (IQSC), University of São Paulo (USP), São Carlos, Brazil.

His work focuses on the design and study of cysteine cathepsin inhibitors aimed at advancing therapeutic strategies for cancer.

Brian N. Lahr was born in Lorena, Brazil, in July 2003. He is pursuing the B.Sc. degree in electrical engineering with emphasis on electronics from the School of Engineering, University of São Paulo (EESC/USP), São Carlos, Brazil.

His research interests include photonic and microwave structures, machine learning techniques, and sensing applications.

Achiles F. da Mota received the Ph.D. degree in electrical engineering from the University of São Paulo, São Carlos, Brazil, in 2019.

From 2022 to 2024, he was a Postdoctoral Researcher at Northeastern University, Boston, MA, USA. He is currently a Professor with the Department of Electrical Engineering, University of Brasilia (ENE/UnB), Brasilia, Brazil. His research interests include metamaterials and metasurfaces for microwave and optical applications, time-modulated nanoantennas, time crystals, and quantum nanophotonics.

Andrei Leitão received the bachelor's degree in pharmacy biochemistry and the Ph.D. degree in chemistry from the Federal University of Minas Gerais, Belo Horizonte, Brazil.

He is an Associate Professor with the Institute of Chemistry of São Carlos, University of São Paulo (IQSC-USP), São Paulo, Brazil, leading the Chemical Discovery Group (CDG). He holds two postdoctoral positions at the University of New Mexico, Albuquerque, NM, USA, and the University of Duisburg-Essen, Germany. He has experience in drug discovery applying cheminformatics, medicinal chemistry, and cell-based assays in cancer.

Vinicius M. Pepino (Member, IEEE) received the Ph.D. degree in electrical engineering from the University of São Paulo, São Carlos, Brazil, in 2023.

He is currently a Professor with the Department of Electrical Engineering and Computing (SEL), School of Engineering, University of São Paulo (EESC/USP). His research interests include photonics, microwaves, and metasurfaces, within the metamaterials group: microwaves and optics (GMeta), with emphasis on holography, biosensors, and devices for communications.

Ben-Hur V. Borges received the Ph.D. degree in electrical engineering from Drexel University, Philadelphia, PA, USA, in 1997.

From 1997 to 1998, he was a Postdoctoral Researcher with São Carlos School of Engineering, University of São Paulo, São Carlos, Brazil. In 2005, he became an Associate Professor with the Department of Electrical and Computer Engineering, School of Engineering, University of São Paulo (SEL/EESC/USP). Since 2018, he has been a Full Professor with SEL/EESC/USP. His research interests include metamaterials and metasurfaces for microwave and optical applications, nanoplasmonics, the design and characterization of devices for communications and sensing applications, and the modeling of optical code multiple access networks.

Dr. Borges is the Director of the Metamaterials Group: Microwave and Optics (GMeta) and an Editorial Board Member of *Journal of Physics: Photonics*.

Coordenação de Aperfeiçoamento de Pessoal de Nível Superior (CAPES) - ROR identifier: 00x0ma614